RESEARCH ARTICLE

NANO · MICRO small
www.small-journal.com

Graphite-Based Bio-Mimetic Nanopores for Protein Sequencing and Beyond

Chandan K. Das and Maria Fyta*

Protein sequencing using nanopores represents the next frontier in bio-analytics. However, linearizing unfolded proteins and controlling their translocation speed through solid-state nanopores pose significant challenges in protein sequencing. In order to address these issues, this work proposes a biomimetic graphite-based nanopore construction. These nanopores feature a nanometer-sized pore with a constriction zone, mimicking the structure of the α-hemolysin protein pore. Our all-atom Molecular Dynamics simulations demonstrate the high practical potential of these nanopores by revealing how their charge state renders them complete ion-selective and generates an electro-osmotic flow. This study shows that this nanopore construction can detect peptides at the single amino acid level by analyzing the ionic current traces generated as peptides traverse the nanopore. The novelty of the proposed nanopore lies in its ability to modulate the hydrodynamic drag induced by electro-osmotic flow, relative to the electro-phoretic force. This investigation reveals that tuning these forces helps to linearize translocating peptides and extend the residence time of individual amino acids at the constriction zone of the pore. This significantly enhances the detection and sequencing efficiency of the pore. Furthermore, the high relevance of the proposed nanopores is underscored for seawater desalination through electrodialysis and extends to ion separation under salinity gradients.

1. Introduction

Nanopores are nanometer-sized apertures that function as single-molecule biosensors and have achieved significant success in label-free single-molecule DNA and RNA sequencing.[1–3] In a typical nanopore sequencing setup, a transmembrane bias potential is applied across the nanopore, allowing for the measurement of longitudinal ionic current traces. As individual analytes pass through the nanopore under the applied potential, they block the flow of ions, which is reflected in the time-dependent current traces through the pore. By analyzing the amplitude and duration of these blockade currents, this technique enables the precise identification of analytes at the single-molecule level, providing a cost- and time-efficient, as well as a label-free method. These nanopores can be created in various ways. Biological nanopores, such as α-hemolysin, aerolysin, and MspA, are embedded in lipid bilayers and formed by the self-assembly of protein subunits.[4–6] In contrast, solid-state nanopores are fabricated from materials like SiO_2, SiN_x, MoS_2, and graphene using laser-based optical etching and electron milling techniques.[7–9]

Building on the tremendous success of nucleic acid sequencing, single-molecule protein sequencing using nanopores is recently gaining significant attention.[10–12] Nanopore sequencing offers the potential for rapid and high-throughput protein analysis, presenting a significant advantage over traditional techniques for example Sanger sequencing[13] and Edman degradation[14], which are time-consuming, expensive, and enzyme-dependent. However, there are several challenges associated with protein sequencing using nanopores due to the complex nature of proteins. One major issue is the strong intramolecular interactions within proteins, which prevent them from threading the nanopore in a single-file, that is as linear chains. Unlike DNA or RNA, proteins have a heterogeneous charge distribution, making it difficult to utilize electro-phoretic force (EPF) for unidirectional transport through the nanopore.[11,15] Additionally, the subtle differences between amino acids pose a challenge for the electrical recognition of individual amino acids.

Within these restrictions, many efforts have been directed towards protein sequencing using nanopores. Among them, Oukhaled and co-workers have achieved a notable success in single-amino acid detection.[16] Their experiments utilizing ionic current detection for all 20 natural amino acids through the aerolysin nanopore, aided by a short polycationic peptide carrier, successfully identified 13 of them. On the other hand, Brinkerhoff *et al.* and Yan *et al.* demonstrated the ability to discriminate single–amino acid substitutions by using a DNA-peptide conjugate, which was pulled through the MspA nanopore by a DNA

C. K. Das, M. Fyta
Computational Biotechnology
RWTH Aachen University
Worrignerweg 3, 52074 Aachen, Germany
E-mail: c.das@biotec.rwth-aachen.de

The ORCID identification number(s) for the author(s) of this article can be found under https://doi.org/10.1002/smll.202407647

DOI: 10.1002/smll.202407647

helicase.[17,18] In these experimental studies, supported by computer simulations, the claim is that the MspA pore does not need to be engineered and read-out is compatible with peptides with either a conjugated N- or C-terminus and only the sample preparation and data analysis need to be selectively changed. The subsequent research by Dekker and co-workers employed a similar setup involving a DNA-peptide-DNA conjugate to read the amino acid composition of the peptide and differentiate between closely spaced phosphorylation sites.[19] In this setup, an additional DNA tag was used to induce EPF drag against the ratcheting motion of the helicase-bound DNA, thereby linearizing the peptide inserted between the DNA fragments.

As an alternative, several previous studies have explored combining EPF with the electro-osmotic flow (EOF) to facilitate a single-file translocation of polypeptides through the nanopores. Theoretically, EOF results from the net flux of water through the nanopore, due to the accumulation of net ionic charge inside the nanopore, and is primarily used for the capture and trapping of molecules within nanopores.[20,21] Li and Muthukumar have systematically modelled the influence of nanopore characteristics on the EOF and protein translocation.[22] Wanunu and co-workers achieved unidirectional single-file protein transport propelled by EOF through an α-hemolysin nanopore by attaching negatively charged polypeptide tags designed to induce EPF drag, in the presence of a guanidinium chloride buffer.[23] A detailed study indicates that exposure of biological nanopores to high concentrations of guanidinium chloride causes the nanopore lumen surface to become positively charged due to the transient binding of guanidinium cations to the protein surface, thus transforming it into a highly anion-selective nanopore that generates EOF.[24] Nevertheless, chaotropic reagents contaminate the electrical signal during nanopore analysis. Other studies have also reported that EOF accelerates the unfolding and translocation of individual polypeptides through an engineered charge-selective α-hemolysin nanopore.[25] Maglia and co-workers recently extended the concept of engineered EOF to drive polypeptides against EPF by introducing a set of negatively charged residues in the lumen of a biological CytK nanopore. These promote the stretching of polypeptides, allowing in this way the recognition of individual amino acids as these pass through the reading head of a nanopore.[26] Recently other protein detection approaches were also reported in the literature.[27–33] These refer to enzyme-assisted peptide sequencing utilizing enzymatic cleavage and nanopore sensing that is based on host–guest interaction-assisted[32] and the read-out of the 20 proteinogenic amino acids and representative post-translational modifications[31] for peptides associated with diseases.[33]

Akin to biological nanopores, solid-state nanopores, particularly those made from 2D materials like graphene and MoS_2, demonstrate its feasibility in protein sequencing.[34,35] Precisely controlling the motion of proteins with DNA-processing enzymes, a method used with biological nanopores, is not possible with solid-state nanopores. However, partial control is achieved in the case of a single-stranded DNA threaded through a graphene nanopore due to sticky hydrophobic interactions between the single nucleobases and the graphene surface.[36] As an alternative, the tuning of EPF and EOF is a promising option for obtaining a controlled motion of protein while traversing nanopores. Additionally, this strategy could turn useful also in imposing single-file translocation of (poly)peptides through solid-state nanopores, even without the need of chaotropic agents. However, this concept has not yet been fully explored for solid-state nanopores.

On the other hand, the ion selectivity of biological pores, originating from the surface charge of the pore lumen, can be mimicked by adjusting the charge of synthetic solid-state nanopores.[24,37–39] This leads to differential binding of ions inside the nanopore lumen, which essentially modulates the molecular flux of water and produces EOF.[22] Besides nanopore sequencing, potential applications of such ion-selective nanofluidic channels were found for the desalination of seawater, known as electrodialysis,[38] and for harnessing blue energy from salinity gradients.[40] Aksimentiev and co-workers investigated the ion and water transport through a graphene-silica-graphene membrane by varying the charge of graphene[39] and in a separate study, through a silica membrane in presence of a guanidinium chloride buffer.[24] It is worth noting that the typical Si-based solid-state nanopores are more than 1 nm thick, making the read-out region too thick to distinguish individual amino acids. In contrast, nanopores made from graphene, an atomically-thick layer of carbon, offer a potential solution to this problem.[34,41]

In this work, inspired by α-hemolysin and its homologous biological nanopores, we propose a novel graphite-based 3D solid-state bio-mimetic nanopore; refer to **Figure 1** showing the respective pore construction. In this design, the constriction zone (which acts as the reading head) halfway along the pore is made of a graphene layer, allowing for the detection of peptides at the single-amino acid level. Additionally, graphite is an electrically conductive material enabling the modulation of the nanopore's charge, thereby generating ion-selectivity and EOF. Using all-atom molecular dynamics (MD) simulations, this study delves into: (a) examining the selective transport of ions and water based on the charge state of the bio-inspired graphite nanopore, with potential applications in water desalination; (b) assessing the feasibility of using EPF and EOF to stretch unfolded proteins within the nanopore; (c) monitoring ionic current traces during the translocation process to evaluate its capability for amino acid sensing. (d) reversing electrodialysis, utilizing only salinity gradients to create a platform for blue energy generation. The insights elicited from our study demonstrate that the proposed bio-inspired 3D graphite-based nanopore can potentially detect proteins at the single-amino acid level, and holds a high promise in other nanotechnological fields, as well. This study additionally highlights the versatile applications of graphite-based nanopores beyond bio-sensing, such as ion-selective devices and seawater desalination. Accordingly, the following discussion will be spread among these applications, rather than focusing on one.

2. Computational Details

All-atom Molecular Dynamics (MD) simulations were conducted to model graphite-based bio-mimetic nanopores submerged in an aqueous solution of 1M KCl using the Gromacs[44] version 2021.5 simulation program. Note that the respective simulations are deterministic and do not account for any stochasticity related with the Brownian motion of the single amino acids and all other species in the modeled systems. The graphite membrane consisted of 21 vertically stacked layers of 10 nm × 10 nm graphene sheets, as constructed using the Carbon Nanostructure

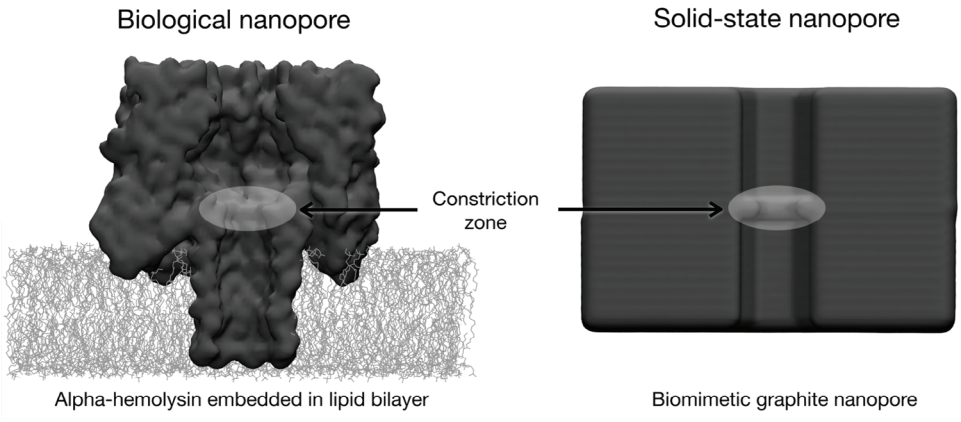

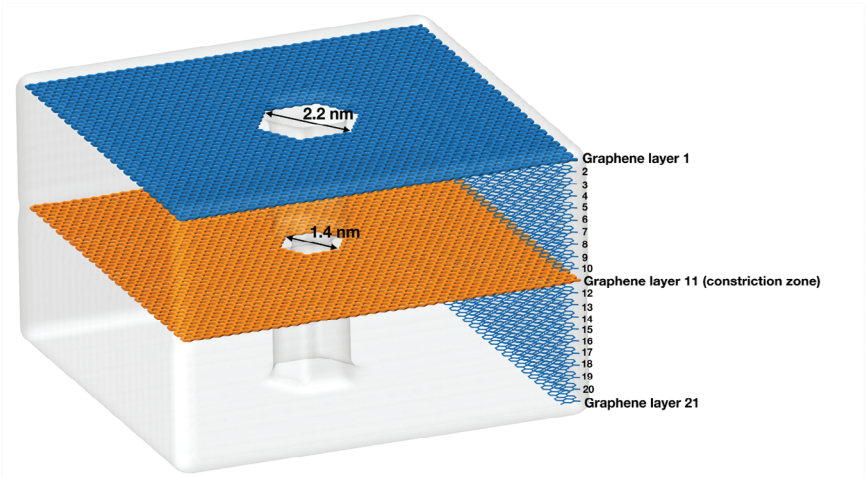

Figure 1. Top panel. A sketch of the proposed graphite-based solid-state nanopore (right) inspired by the α-hemolysin biological nanopore (left). Both nanopores are depicted as cut-away molecular surfaces to reveal the presence of a constriction zone (approximately 1.4 nm in diameter) in the pore lumen. The atomic coordinates of α-hemolysin were obtained from the Protein Data Bank (access code: 7AHL.pdb[42]). Using the CHARMM-GUI[43] webserver, a lipid bilayer was added around the nanopore for a more intuitive representation. Bottom panel. A schematic diagram illustrates the molecular fabrication of the proposed nanopore, constructed using 21 vertically stacked layers of graphene. The topmost (in blue) and middle (in orange) 10 nm × 10 nm graphene layers are fully shown in the figure, while the remaining layers are only partially shown for clarity. The nanopore constriction is located in the middle layer.

builder plugin of the Visual Molecular Dynamics (VMD)[45] editor. Following this, a circular nanopore was crafted by deleting atoms satisfying $x^2 + y^2 < R^2$, where x and y are the coordinates of the atoms, and R is the target radius of the opening. The radius of the lumen was set to 1.1 nm, and the radius of the constriction zone, located halfway along the pore, was set to 0.7 nm, resulting in a constriction aperture with a diameter of 1.4 nm, closely resembling a biological α-hemolysin nanopore. The schematic diagram in Figure 1 illustrates the bio-inspired graphite nanopore proposed in this work. This pore will be used throughout in our simulations. The carbon atoms of the graphite nanopore were modeled as aromatic carbon (ca atom type), with force field parameters described by the generalized Amber force field (GAFF).[46,47] In order to investigate selective ion transport, a positively charged nanopore was created by assigning a charge of 0.001 to each graphite carbon atom, yielding surface charge density of 0.006 C m^{-2}. Conversely, a negatively charged nanopore was modeled using a negative charge of the same magnitude. The nanopore was placed in a simulation box measuring 10 × 10 × 12 nm, which was then filled with 17622 TIP3P[48] water molecules. 80 K^+ and 80 Cl^- ions were added to neutralize the net charge of the negatively charged and positively charged nanopore systems, respectively. Additional 752 K^+ and 752 Cl^- ions were added to achieve a 1M KCl electrolyte solution, bringing the total number of atoms in each system to 134052. Periodic boundary conditions were applied in all directions. We also modeled a system using a neutrally charged graphite nanopore in a similar manner. For this system, the carbon atoms in the graphite were considered to be neutral in charge.

Prior to the MD simulations, each system underwent energy minimization for 1000 steps using steepest descent algorithm. Harmonic position restraints with a force constant of 10000 kJ mol^{-1} nm^{-2} were applied to all graphitic carbon atoms, maintained throughout the subsequent MD simulations. All systems were then heated from 0 to 300 K over 2 ns of MD simulation at a canonical (*NVT*) ensemble. This was followed by a 10 ns equilibration at an isobaric-isothermal (*NPT*) ensemble. The temperature was maintained at 300 K using a velocity rescaling[49]

thermostat with a coupling time constant of 0.1 ps. A semi-isotropic pressure coupling allowing independently coupling the lateral (xy) directions and the normal (z) direction to a pressure bath, was applied with a weak coupling Berendsen[50] barostat (time constant of 5 ps and compressibility of 4.5×10^{-5} bar^{-1}). This allowed the system to equilibrate along the z direction, maintaining a pressure of 1 bar. Non-bonded Coulomb and van der Waals interactions were treated with a buffered Verlet pair list,[51] with potentials smoothly shifted to zero at a 1.2 nm cut-off. Beyond that, the particle mesh Ewald (PME)[52,53] method was used for the calculation of the long-range electrostatic interactions with the default settings implemented in Gromacs. The SETTLE[54] algorithm constrained the internal degrees of freedom of water molecules, while the LINCS[55] algorithm constrained all bonds involving H atoms, allowing an integration with a 2 fs time step using the leap-frog algorithm. Following equilibration, 100 ns production simulations under an applied electric field were performed at a *NVT* ensemble, using the average dimensions of the system obtained during the *NPT* equilibration. The electric field strength (**E**) is defined as $\mathbf{E} = V/l_z$, where V represents the target transmembrane bias and l_z is the length of the simulation cell along the z direction.[56] The transmembrane voltage, V was set to –1 V and was consistently used throughout all applied electric field simulations conducted in this study. Note that this field strength is higher than the typical voltage range used in the experiments. As common in atomistic MD simulations, larger voltage values are needed and are set in order to reach desired time scales or realize—otherwise slower—processes.

The water desalination (electrodialysis) simulation was modeled by placing two identical graphite nanopores positioned 6.4 nm apart, with their pore axes aligned. One nanopore was positively charged, and the other was negatively charged. These nanopores were placed in a $10 \times 10 \times 25$ nm simulation box and were solvated with 41582 water molecules. 755 Na^+, and 755 Cl^- ions were added to produce a 0.48 M NaCl solution, mimicking the salinity of seawater. The simulation parameters and protocols were consistent with the initial setup presented above. After minimization and equilibration, 200 ns all-atom MD simulations were conducted under an applied electric field at a *NVT* ensemble. Starting from the last frame of the electrodialysis simulation, a reverse electrodialysis simulation was conducted for 20 ns without applying a transmembrane bias potential. The charges of the positively and negatively charged pores were maintained as discussed above. In this setup, though, an additional 10×10 nm single graphene layer was introduced to separate the catholyte from the anolyte in this setup. The simulations of seawater desalination and ion separation under a salinity gradient were repeated twice more, each time starting with different random initial velocities.

In order to model the protein sequencing simulation, an initial structure of the model protein with the sequence of N′-$K_{20}(GGK)_{23}$-C′ was built using the tleap module in Amber and threaded through the nanopore. The polycationic lysine (K_{20}) tag was designed to induce EPF along an electrical gradient. The Amber ff14SB[57] force field was utilized to describe the protein, while the parameters for the positively charged nanopore were identical to those used in previous setups. The protein-nanopore system was placed in an electrically neutral 1M KCl electrolyte solution contained within a periodic box of $10 \times 10 \times 20$ nm, resulting in a total of 216663 atoms with 44403 water molecules, 1266 K^+ ions, and 1387 Cl^- ions. Upon assembly, we conducted MD simulations using the same MD protocols as used for the previous simulations. Additional harmonic position restraints (force constant of 1000 kJ mol^{-1} nm^{-2}) were applied to the protein C_α atoms located within the nanopore lumen during the initial *NVT* and *NPT* equilibration phases, allowing the protein above and below the graphite nanopore to relax and adhere to the graphite surface. A 1.5 µs production simulation was then carried out under the applied transmembrane voltage of –1 V to simulate the translocation of the protein through the nanopore. We conducted an independent 1.5 µs repeat production simulation with a different set of random velocities, which provided similar results. This setup was further used to calculate the ionic current traces through the nanopore for all 20 natural amino acids and a cancer-associated posttranslationally modified lysine typically found in histone proteins. Besides that, in order to estimate the extent to which the charge state of nanopore affects translocation speed, we also conducted an additional 1.5 µs MD simulation of protein translocation through an electrically neutral graphite nanopore with an applied transmembrane bias of –1V.

For assessing the ionic current for each individual proteinogenic amino acids, we selected a frame from the translocation simulation, where the K32 residue was precisely positioned at the pore's constriction zone. At this frame, all C_α atoms of the protein were restrained, allowing only the protein side chains to move, ensuring that the protein did not translocate during the applied electric field simulation. The purpose of this setup is to enable the recording of the blockade ionic current signatures of the residue residing at the pore. The K32 residue was then mutated separately to each individual amino acid. The number of counter ions were adjusted accordingly to maintain net charge neutrality. We carried out the energy minimization, followed by a short 200ps *NPT* equilibration. Subsequently, 50 ns MD simulation under the applied electric field was conducted. These steps were repeated for each mutation.

In our analysis, we primarily focused on the time-dependent ionic current traces to determine whether the total current was predominantly due to cations or anions of the electrolyte, which in turn defines the strength and direction of the EOF. Additionally, we analyzed the amino acid composition of the protein based on their ionic current signatures. The instantaneous ionic current, $I(t)$, was computed as

$$I(t) = \frac{1}{l_z \Delta t} \sum_{i=1}^{N} q_i \left[z_i(t + \Delta t) - z_i(t) \right] \quad (1)$$

where i sums over all ions, l_z is the box-dimension along the z-axis, Δt is the time between subsequent frames (set to 10 ps), z_i is the z-coordinate, and q_i is the charge of the ith ion.[56] Instantaneous current traces were block-averaged over 100 ns to reduce noise. The average ionic current was calculated by summing $I(t)$ for all frames and dividing by the total number of frames. We also calculated the average ion and water flux, defined by computing the molecular flux through a defined plane, for these nanopores. In addition, ion concentrations (monitored through number

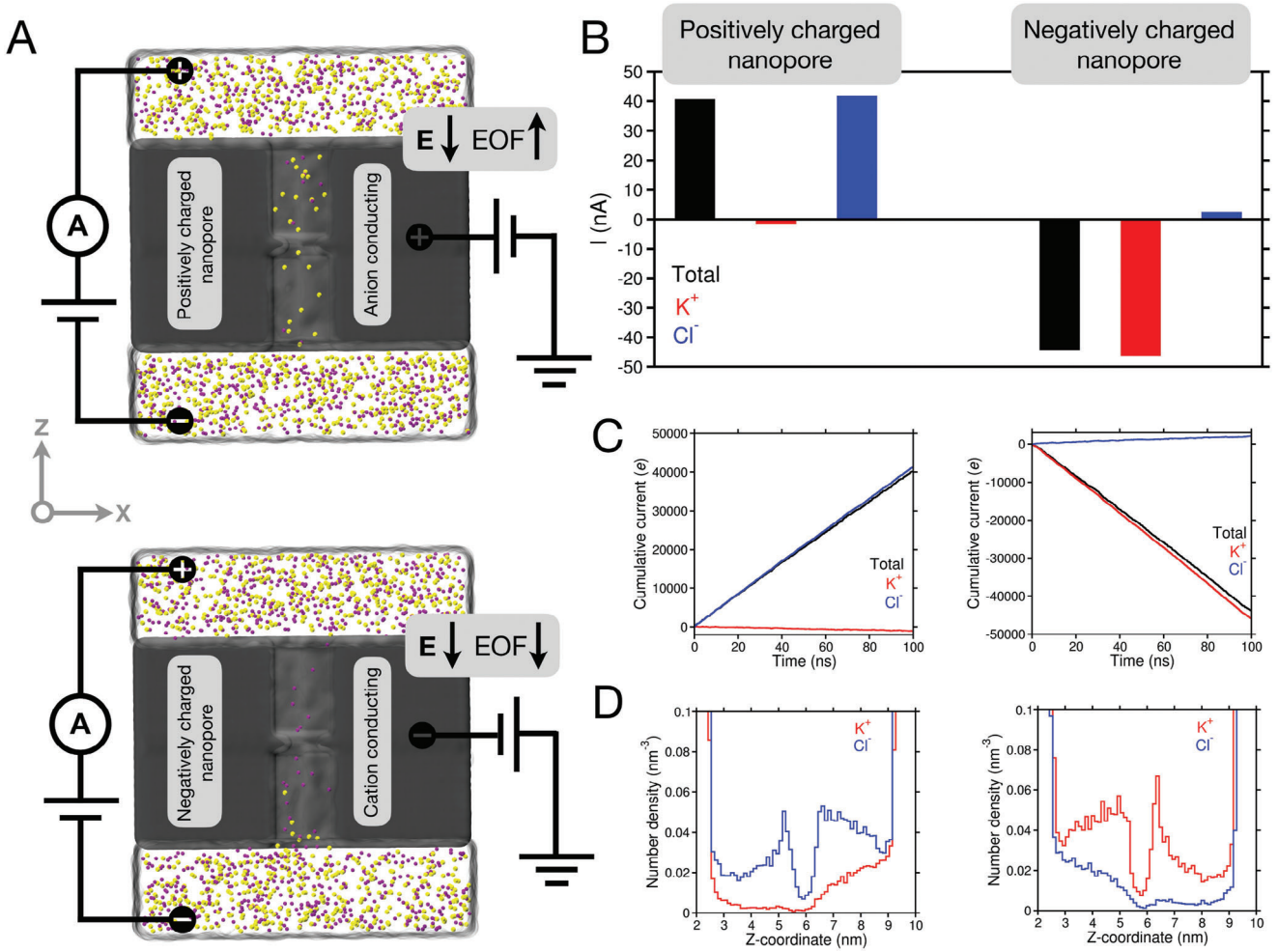

Figure 2. A. The setup of a positively (top) and a negatively (bottom) charged graphite-based bio-mimetic nanopore submerged in a 1M KCl electrolyte. The molecular surface of the pore lumen is represented in a cut-away view (dark gray), while the transparent molecular surface illustrates the aqueous KCl solution. The K^+ and Cl^- ions are depicted as purple and yellow van der Waals spheres, respectively. The direction of the applied electric field, **E** and the induced EOF in each case are indicated. B. The average instantaneous ionic current, C. the cumulative ionic current, carried by the ionic species, and the D. average ion distribution inside the pore lumen over the course of the MD simulation. In panels B–D, the results for both types of ions and their sum ('Total') in the two different nanopores under a transmembrane voltage of –1V for the 1M KCl solution are shown. The charge state of nanopores are indicated at the top.

densities) along the pore axis (*i.e.*, *z*-axis) were evaluated at different stages of the simulations.

3. Results and Discussion

3.1. Ion Selective Nanopore Induces EOF

Our investigation commences by unraveling the ionic transport properties of the bio-mimetic graphite-based nanopores as illustrated in Figure 1 under the applied electric field. In the respective setup, depicted in **Figure** 2A, the graphite-based nanopore is submerged in a 1M KCl electrolyte solution. A transmembrane voltage is applied to create a potential difference across the nanopore, inducing ion flow between the two electrolyte-filled compartments and generating an ionic current. Additionally, an independent voltage source (also sketched in Figure 2A) modulates the charge state of the graphite nanopore. With this setup, we investigate the influence of the charge state of the nanopore on the ion selectivity, that in turn induces the EOF under the transmembrane bias potential. As presented in the following, the EOF can in turn be tuned for target applications ranging from protein sequencing to desalinating seawater. We conducted MD simulations under an applied transmembrane bias potential of –1V for two different charge states of the nanopore and computed the cation-conducting current, the anion-conducting current, and their total contribution in the instantaneous ionic current and the cumulative current provided in Figure 2B-D.

The ionic current values in Figure 2B clearly show that for a positively charged nanopore, the average anion-conducting current dominates the average total current, contributing +102.7% of the total current. In contrast, the average cation-conducting current contributes –2.7% to the total current. In fact, these findings are corroborated by the slopes of the cumulative currents carried by ion species through nanopore over the course of MD

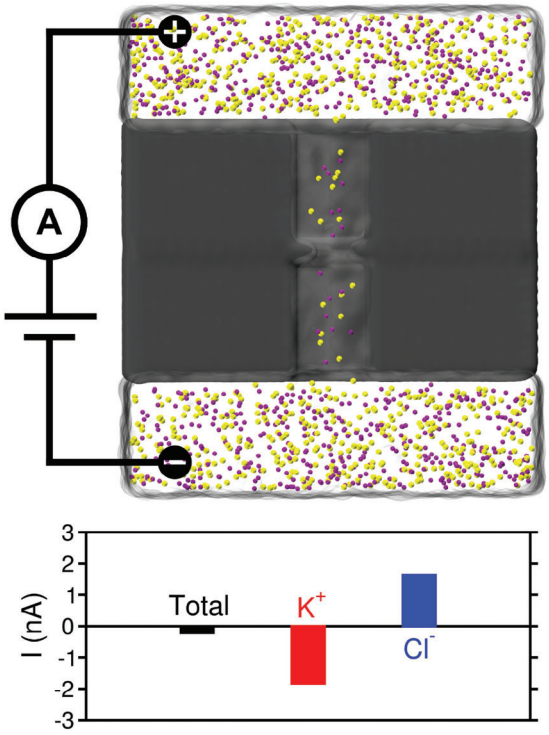

Figure 3. Top-panel. The setup for a neutral graphite nanopore. Bottom-panel. The average instantaneous ionic currents carried by K^+ and Cl^- ions in a 1M KCl solution under a transmembrane bias potential of −1V.

simulation as shown in Figure 2C. The negative slope of the cation-conducting current for the positively charged nanopore suggests their negative contributions to the total ionic current. On the other hand, inverse trends are observed for a negatively charged nanopore. The nearly identical slopes between the total and anion-conducting currents for the positively charged nanopore, as well as between the total and cation-conducting currents for the negatively charged nanopore (see Figure 2C), indicate that these ions fully contribute to the total nanopore current. Besides that, the magnitude of the ionic current generated in the charged graphite nanopores is significantly higher than that of the neutral graphite nanopore presented in **Figure 3**, in which the additional membrane voltage is not applied inducing nanopore neutrality. This indicates a superior performance of the charged graphite nanopore in facilitating ionic transport, potentially offering enhanced efficiency for applications requiring high ionic conductivity. These findings are in line with previous reports on graphene-silica-graphene membrane with varying graphene charge-states.[39]

Further analysis of the ion distributions computed as number densities of ions along the nanopore's normal (*z*-axis) in Figure 2D reveals the anion-selectivity of a positively charged pore over the the cation-selectivity of a positively charged pore. It is worth noting that the number density of anions reduces significantly at the constriction zone of the positively charged pore under the given transmembrane potential, indicating a significant potential drop at the pore's constriction. A similar density profile is noted for cations in the negatively charged pore in Figure 2D. Interestingly, nearly no cations pass through the positively charged pore, and no anions pass through the negatively charged pore under the given conditions, implying that the setup achieves exclusive ion selectivity, either for cations or anions. However, we did not observe prolonged binding of ions on the nanopore lumen surface leading to ionic current rectification reported for polymer and silicon based nanopores.[58,59] Under the given transmembrane voltage, the nanopore produces the same magnitude of ionic currents regardless the charge state of the nanopore (refer to Figure 2B), ensuring that the ionic current rectification does not occur in this nanopore model. In fact, depending on the nanopore charge state, the cations or anions are electrophoretically driven through the charged nanopores together with a giant water flux (reflected by an average of 360 and 584 water molecules/ns for positively and negatively charged nanopore, respectively). This substantial unidirectional water flux generates an EOF in the direction of the particular ion flow as can be inspected in **Figure 4** for the water and ion flux. For the positively charged nanopore, the direction of the EOF is opposite to the electric field, **E**, while for the negatively charged nanopore, the EOF

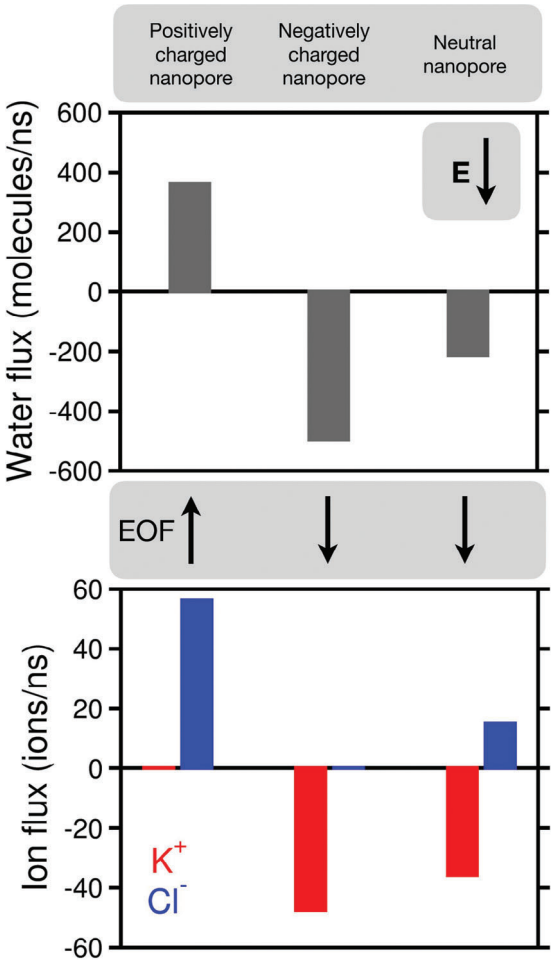

Figure 4. The average water (top panel) and ion (bottom panel) flux through nanopores in the different charge states: positively charged, and negatively charged, and neutral, as indicated at the top. The directions of the electric field, **E** and the EOF are also indicated through the respective arrows.

direction is parallel to **E**. Notably, in the case of a neutral pore, an insignificant resultant water flux is observed due to the difference in diffusivity between K^+ and Cl^- ions. This difference leads to a net flux of K^+ ions, which in turn drives a water flux in the same direction as the K^+ ion movement. Given that the electric field (E) is applied along the $-z$ direction, the K^+ ions move in the $-z$ direction, resulting in a negative water flux. These trends offer a simple but precise and tunable approach to adjust the strength and direction of the EOF by varying the membrane voltage under a given transmembrane bias. In order to explore this further, we conducted additional simulations with higher graphene carbon atom charges. Two independent simulations were performed with carbon charges of +0.0012 and +0.0015 under transmembrane bias of –1V, and the average water flux was estimated. The simulation results show that the water flux, representing the strength of EOF, enhances with the increasing nanopore charge magnitude (see Figure S1, Supporting Information), demonstrating the potential for fine-tuning the graphene carbon atom charge to optimize the strength of the EOF.

3.2. Protein Detection at the Single Amino Acid Level

The efficiency and potential impact of these proposed graphite-based bio-mimetc nanopores is further emphasized in view of protein detection at a single amino acid level. It is noteworthy that the nanopore-based protein sequencing must address several key challenges, including protein unfolding, controlled translocation speed, and reliable detection of all 20 amino acids and their post-translational modifications.[11,15] The EOF exerts a hydrodynamic drag that, which can be tuned together with the electric field induced EPF drag in order to linearize (i.e., open or unfold the 3D structure of) translocating peptides and control the respective translocation speed in view of protein detection and sequencing. The role of the EOF in the translocation of biopolymers through different types of biological and solid-state nanopores has been analyzed in detail.[22] In this study, we demonstrate the interplay of this with the EPF and the respective potential to tune this with a highly positively charged model polypeptide, N′-$K_{20}(GGK)_{23}$-C′, threaded through a positively charged graphite nanopore; see **Figure 5** for the schematic illustration of the nanopore setup for protein detection considered in this work. Note that, by lowering the pH below 3, the Asp and Glu residues become neutral. Through this, a positively charged or at least neutrally charged polypeptide chain can be achieved, without affecting the chemistry of the graphite nanopore. In this setup, the additional N-terminal poly-lysine (K_{20}) tag is introduced to enable the translocation. Specifically, due to its high charge it experiences a strong EPF drag due to the transmembrane bias potential, thus driving the target peptide (–$(GGK)_{23}$–) through the nanopore along the electric field. Simultaneously, the hydrodynamic drag, acting opposite to the EPF, due to the EOF provides a subtle molecular friction on the peptide residues within the pore lumen, helping to overcome the barriers associated with protein stretching and facilitating the linearization of the protein inside the pore lumen.

MD simulations were performed with this setup, immersed in a 1M KCl solution under a transmembrane voltage of –1V. Throughout the simulation, the $(GGK)_{23}$ part of the protein chain adheres to the surface of the graphite nanopore. Specifically, the

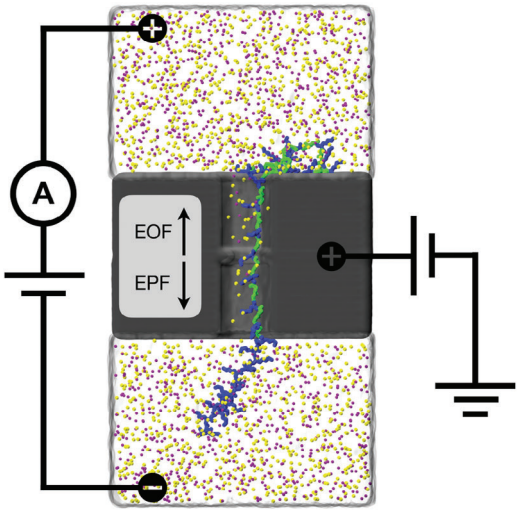

Figure 5. The nanopore setup for protein detection considered in this work. A voltage difference across the chambers induce an electric field at the pore region, while another applied voltage can charge the 3D pore material, as indicated by the two sources. A polypeptide chain with a sequence of N′-$K_{20}(GGK)_{23}$-C′ is threaded half-way through the positively charged nanopore, immersed in a 1M aqueous solution of KCl. The peptide is shown using stick representation coloured according to the residue type (lysine (K) is blue and glycine (G) is green) and the nanopore is shown as a cut-away molecular surface in gray. K^+ and Cl^- ions are shown in purple and yellow spheres, respectively. A transmembrane bias potential of –1V is applied to induce EPF drag acting opposite to EOF, as indicated by the arrows.

backbone carbonyl oxygen atoms form direct contacts to the positively charged graphite surface. However, the positively charged lysine side chains do not form contacts with the membrane due to the strong repulsive Coulombic interactions involved. For the same reason, the high positively charged residues of the N-terminal poly-lysine (K_{20}) tag, also do not form any contacts to the positively charged nanopore surface. Instead, this poly-cationic N-terminal remains fully solvated. In order to determine whether the protein maintained its stretched conformation during the non-equilibrium MD simulation with an applied electric field, the distance between the C_α atoms of K26 and K38 was monitored throughout the simulation; see **Figure 6A**. Interestingly, the time trace of the K26:C_α···K38C_α distance clearly indicates that the part of the peptide inside the pore lumen maintained a stretched conformation during the applied electric field simulation, as we anticipated. This trend clearly demonstrates that the tug of war between the hydrodynamic drag and the EPF drag on the peptide leads to the linearization of the unfolded peptide inside the charged solid-state nanopore. This observation completely aligns with previous reports using a dynamic biological CytK nanopore.[26] Furthermore, since this straightening phenomenon is independent of the peptide sequence intended for sequencing, a similar observation can be expected in the case of real proteins.

The step-wise movement of peptide chains is vital for an efficient protein read-out using nanopores. Extended pauses at specific positions enable longer ionic current measurements, enhancing the accuracy of pore content identification. Additionally, controlled pausing during nanopore translocation can facilitate

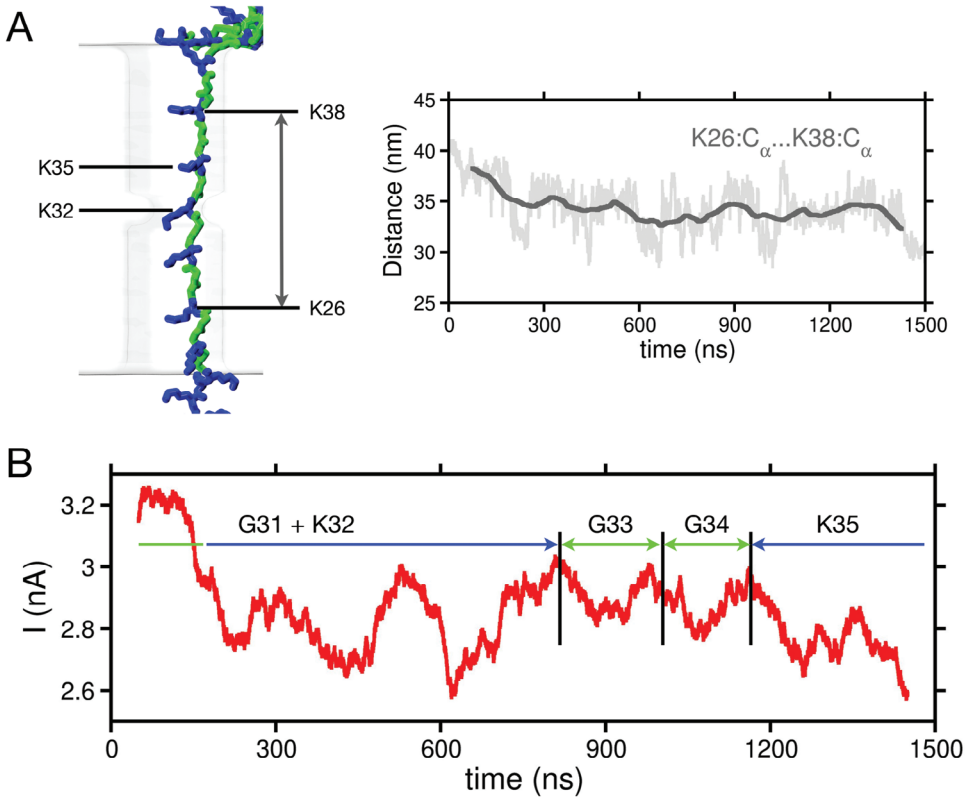

Figure 6. A. The stretching, i.e., linearization, of the peptide inside the pore lumen is monitored by the distance between the C_α atoms of K26 and K38 throughout the 1.5 µs MD simulation. B. The time traces of the blockade current, presented as a running average computed in consecutive 100 ns windows monitor the translocation of the $K_{20}(GGK)_{23}$ peptide through the pore. The blockade regions corresponding to the passage of specific residues (residue name and index) are indicated by the arrows and the legends. The ionic current traces obtained from an independent repeat simulation of peptide translocation is provided in Figure S6 (Supporting Information).

the determination of the peptide sequence from the ionic current data. In view of these points, we monitored the translocation events of the peptide throughout the MD simulation under the applied electric field and calculated the time traces of the ionic current during translocation. Note that, the overwhelming EPF drag on EOF drives the peptide through the nanopore along the direction of the transmembrane electric field **E**. Note that we focus on the concept of the interplay between the EPF and the EOF in the nanopore and not the exact quantification of their relation, which can be handled more efficiently by using mean-field approaches involving the Poisson–Nernst–Planck and/or the Smoluchowski–Poisson–Boltzmann equations.[22,60] In order to provide, though, with a rough quantitative estimate of this interplay, we rely on the calculations of the the average water and ions fluxes discussed above and are directly related to the EOF and EPF, respectively. In order to neutralize, for example, the EOF caused by an average water flux of 360 molecules/ns in a positively charged pore, a flux of approximately 56 K^+ ions/ns generating the EPF (moving in the opposite direction to 56 Cl^- ions/ns) is required. Accordingly, under a field strength of 1V, the EPF needs to be roughly 17.5 % of the EOF in order to balance the EOF and linearize the protein. In other words, 7 K^+ ions can balance 40 water molecules per nanosecond.

The simulation shows that a total of five residues namely G31, K32, G33, G34, and K35 of the peptide pass through the constriction zone of the pore in 1.5 µs simulation time (refer to Figure 6B). This corresponds to a translocation speed of roughly 0.15 msec for a short peptide of 500 amino-acids within the uniform translocation time per residue approximation. The exceptional long residence time at the constriction zone for each translocating residue, which is so far only achieved with biological nanopores using DNA processing enzymes for DNA-protein conjugates,[17–19] originates on the EOF-induced hydrodynamic friction acting against the EPF drag in the positively charged solid-state nanopores. Accordingly, the signal-to-noise ratio of the nanopores is expected to be enhanced. In contrast, in the absence of the hydrodynamic friction induced by the EOF, the EPF-guided translocation rate of the protein through 2D graphene nanopores is substantially higher, blurring the ionic signatures of individual amino acids in the protein.[34] Interestingly, our nanopore setup enables the distinct identification of blockade current profiles for the translocated lysine and glycine residues; see Figure 6B. Figure 6B demonstrates that the current blockades and their duration are directly correlated to the excluded volumes (steric sizes) of lysine and glycine residues. The sterically bulkier lysine residue blocks more ionic flow compared to the glycine residue, resulting in a larger drop in the blockade current of lysine and at the same time, also longer blockade duration. Thus, our study potentially paves the way to regulate the protein translocation rate through nanopores by selectively utilizing the

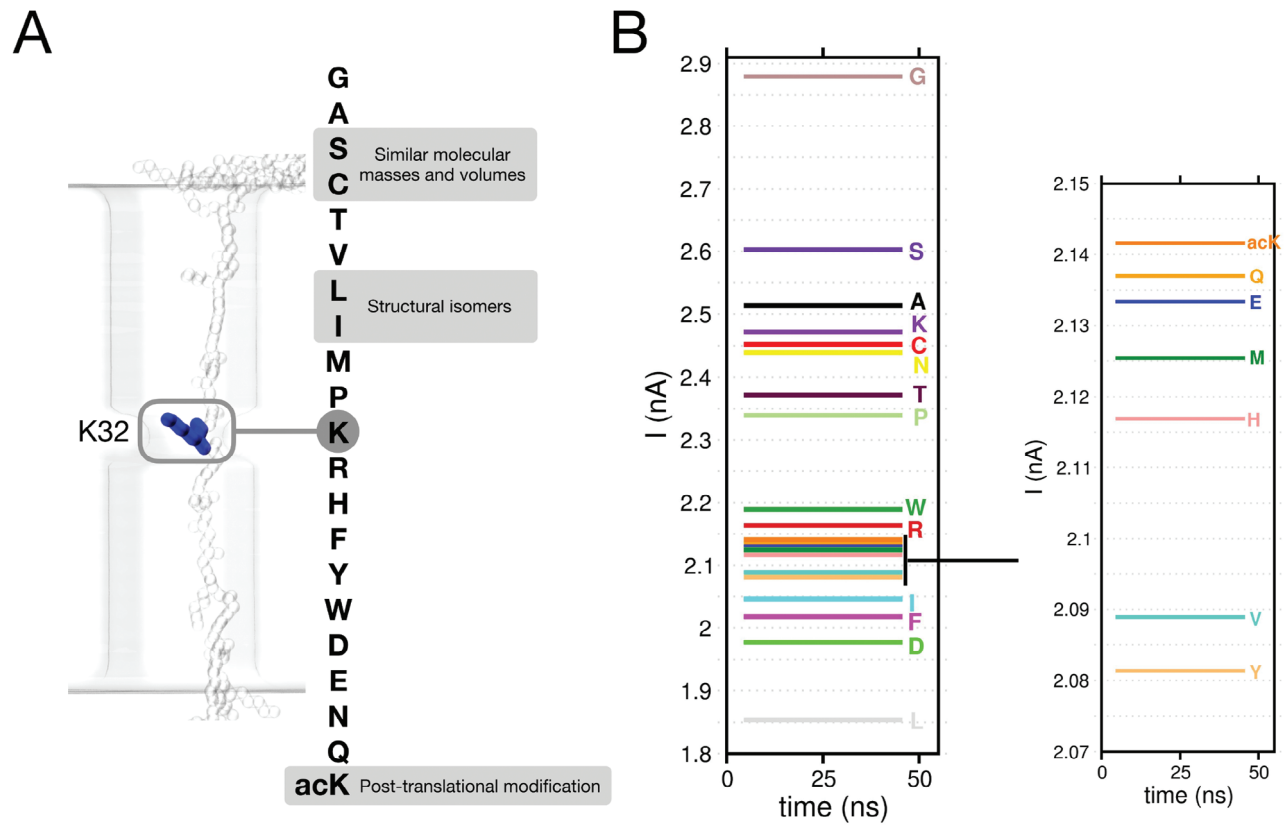

Figure 7. A. The sketch of a peptide threaded through the pore illustrating individual mutations to all proteinogenic 20 amino acids and a post-translationally modified acetylated lysine (denoted as acK) at the position 32 as indicated in the figure. The structurally very similar Ser (S) and Cys (C) residues, the structural isomers Leu (L) and Ile (I) residues, and the post-translationally modified acetylated lysine (acK) residues are also highlighted in the figure. B. The superimposed average ionic current values obtained from the individual simulations performed for each of the 21 peptides are summarized in this figure. At the far right, part of this current spectrum is zoomed in to reveal the differences at the sub-nA level. The errors in the estimation are provided in Figure S2 (Supporting Information).

competition between the EPF and the EOF. This in turn strongly enhances the efficiency in resolving proteins at the single amino acid level. This figure highlights the differences in the calculated blockades with respect to the type and the combination of amino acids threading the constriction zone. In this sense, the transport of only G reveals shallower blockades than the combination of K and G. In this case, the presence of K decreases further the current. These trends can guide further investigations to fine tune the read-out.

In order to briefly address the influence of the EOF on the translocation process we bring again in attention previous reports on the generated electroosmotic flow in CytK biological nanopores that induces the unidirectional transport of unstructured natural polypeptides against a strong electrophoretic force facilitating linearization of proteins and a unidirectional translocation.[26] These reports strongly highlight how the EOF drag counteracts that of the EPF. We assess and confirm this in our simulations by repeating the peptide translocation under the same applied voltage of -1V, but remove the pore charges. In this way, we technically switch off the EOF and observe that 16 amino acids passed through the nanopore constriction zone within a 1.5 μs simulation period, implying a translocation speed of 0.047 ms for 500 amino acids, which is significantly higher than that observed with a positively charged pore. This clearly demonstrates the high importance of the EOF in controlling the translocation process.

The feasibility of detecting and characterizing all 20 proteinogenic amino acids has been previously reported by Oukhaled and co-workers[16] using a wild-type aerolysin biological nanopore and a short polycationic carrier. The solid-state charged graphite-based bio-mimetic pore proposed here, is expected to show a similar feasibility due to the controlled translocaiton and the prolonged capture of the individual residues at the pore constriction, discussed above. We present evidence that our bio-mimicked charged graphite nanopore can distinguish all 20 natural amino acids in **Figure 7**. These amino acids are broadly classified as electrically charged (namely K, R, D, E), hydrophobic aromatic (namely W, F, Y), polar uncharged (namely H, Q, N, T, S, C), hydrophobic non-aromatic (namely L, I, V, G, A, P, M). We also consider a posttranslationally modified acetylated lysine (acK) considered as a biomarker for cancer detection[61] to emphasize the potential of the nanopore in identifying epigenetic markers. In order to unravel the difference in the ionic signatures of all these amino acids, a frame was chosen from the previous translocation simulation, in which the K32 residue was precisely located at the pore constriction. All C_α atoms of the protein were then

restrained, allowing only the protein side chains to move. In this way, it was ensured that the protein did not translocate during the applied electric field simulation, but remained at the pore constriction enabling the recording of the respective ionic blockade for the respective residue. The K32 residue was then mutated to each individual amino acid and a MD simulation was performed as implied in Figure 7A. Note that our amino acid identification strategy provides a qualitative assessment of the detection potential of the charged graphite-based biomimetc nanopore.

The average blockade current recordings obtained from the individual simulations for all mutations, lie within a 1 nA range and clearly show that the among 20 amino acids, G, S, A, K, C, N, T, P, W, R, I, F, D and L produced distinct current blockade signals; see Figure 7B. In contrast, the average blockade currents of the remaining 6 peptides collected into two groups (Q, E, M, H) and (V, Y) lie all in a range of 0.06 nA and could only be resolved with pA recordings. However, the average current blockade of these 6 amino acids were distinctly different from the rest. Interestingly, our nanopore can differentiate between structurally isomeric amino acids, namely leucine (L) and isoleucine (I), with the same molecular mass, based on their blockade currents. Likewise, serine (S) and cysteine (C) with similar molecular masses and volumes produce distinguishable blockade currents. It is important to note that these pairs of residues differ by only a few atoms from each other. The differentiation in the ionic current for each pair of residues arises purely from their steric volumes. For example, the S_γ atom in the cysteine residue blocks ion flow to a greater extent than the O_γ atom in the serine residue. Additionally, in the strategy employed here, the residence time of the residue at the nanopore is effectively infinite, as translocation is halted. This allows for extended recording of the ionic current traces, which increases the signal-to-noise ratio, enabling the distinction between these two structurally isomeric residues based on their average ionic current. Note that this approach relies on the specific structural and characteristics of all amino acids, their isomers, and mutations and differs from other approaches that focus on detecting the shape of entrapped peptides in the pore.[27] However, glutamate (E) and glutamine (Q) produce nearly identical ionic current with this setup, pointing to a further tuning of the setup. Importantly, the charged graphite nanopore construction successfully detected subtle changes of around 0.3 nA due to post-translational modifications, as evidenced by the different current blockades of natural lysine (K) and posttranslationally modified lysine (acK). The zoomed-in window in Figure 7B points to the use of recording equipment that can resolve pA currents, as in the case of biological nanopores. Note that in this figure, the ionic current does not refer to the full configurational space of each amino acid, since the backbone was restrained. In order to resolve the whole spectrum of the ionic currents obtained from all possible molecular configurations is not the scope of this work and has been reported elsewhere.[62,63]

3.3. Desalination of Seawater by Electrodialysis

Such exclusive ion-selective membranes also play a pivotal role in the electrodialysis, which is an advanced desalination and purification technique applied in drinking water production and industrial wastewater reclamation.[64–66] This process utilizes an electric field to drive the separation of ions from sea water through selectively permeable membranes, which are configured to allow either cations or anions to pass through while blocking the opposite charge. The setup typically consists of alternating cation and anion exchange membranes placed between two electrodes, as illustrated in **Figure 8**. This is similar to the configuration used in nanoscale ion pumps based on voltage-gated, ion-selective biological water channel aquaporins. These pumps are capable of efficiently transporting ions from one solvent chamber to another against their chemical gradient, in response to an alternating electric field.[67]

A previous study by Chen and co-workers emphasized the feasibility of charged graphite nanopores in seawater desalination.[38] In this work, authors reported that the graphite-based nanopores with surface charge densities ranging from –0.09 to –0.12 C m^{-2}, diameters less than 3.5 nm, and membrane thicknesses of 8–10 graphene layers demonstrate optimal

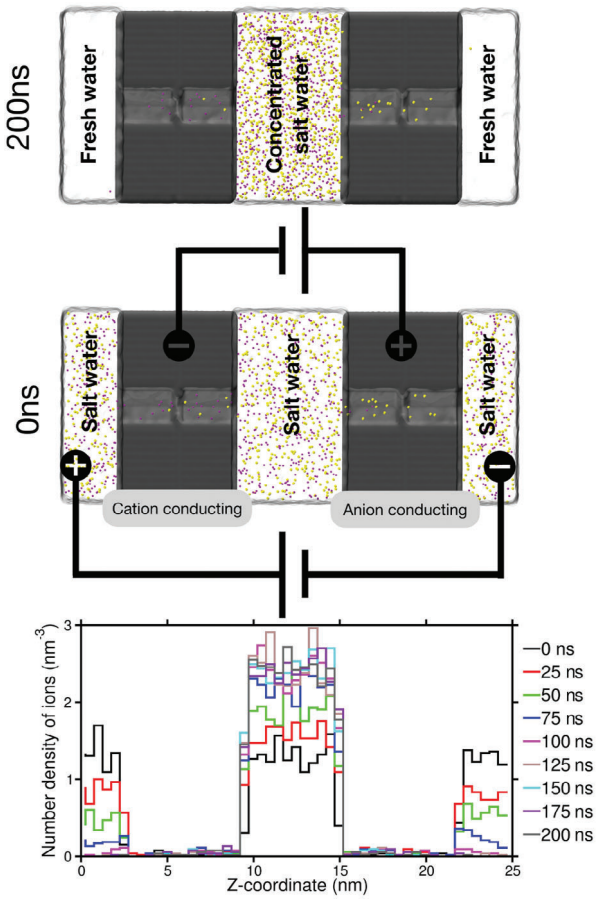

Figure 8. Snapshots referring to the electrodialysis of salt water at the beginning and the end of the process (see indicated times on the right). The electrodialysis setup relies on alternating cation- and anion-conducting graphite nanopores placed within two electrodes. The simulation box is filled with a 0.48M NaCl electrolyte solution, closely mimicking seawater. After applying an electric field, all ions are collected in the middle chamber shown in the top panel. The color coding of the pore and the ions follows that of Figure 2. The bottom panel depicts the number densities of the Na^+ and Cl^- ions along the pore's axis (*i.e.*, z-coordinate) at different stages of the process, as described in the legend.

performance in ion selectivity. Our proposed bio-inspired nanopore constructions, with a much lower surface charge density of 0.006 C m^{-2}, differentiating from previous approaches (see Table S1, Supporting Information, for a list of technical characteristics of comparable studies).

In the following, we assess the potential of such nanopore constructions also in the desalination process. For this, we carried out MD simulations to model the electrodialysis process for 0.48M NaCl solution, closely mimicking the salt concentration in the seawater. When an electric field is turned on, we observed that the negatively charged cation-conducting pore collects Na^+ ions, while the positively charged anion-conducting pore collects Cl^- ions, trapping them in the middle chamber between the two ion-selective membranes shown in Figure 8. The ion distribution along the pore's axis (*z*-axis) at various stages of the simulation shows the accumulation of ions in the middle chamber during the electrodialysis process and subsequently the depletion of ions concentration from the cathode and anode chambers; see the bottom panel in Figure 8. Interestingly, the ion number densities in the middle chamber converge after 100 ns, indicating that nearly all ions are concentrated in the middle chamber within this time frame. These results are successfully reproduced in two additional simulations; see Figure S4 (Supporting Information). This strongly demonstrates a highly efficient desalination of salt water and the production of fresh water in the cathode and anode chambers. Thus, we achieve nearly complete ion rejection using charged biomimetic graphite nanopores with a pore area of 3.8 nm^2 (1.5 nm^2 at the pore constriction zone) and a surface charge density of 0.006 C m^{-2} through electrodialysis. For a comparison of the efficiency, previous studies demonstrated that MoS_2 membranes, with pore areas between 0.2 and 0.6 nm^2, rejected 88% of ions through reverse osmosis which is another widely used water desalination method.[68] It is worth noting that in the electrodialysis, it is the charge of the pore that drives the salt separation from the electrolyte solution. Technically, this differs from the reverse osmosis process. In the process of reverse osmosis, the effectiveness of salt rejection and water permeation is significantly influenced by the diameter of the pores and the chemical properties of the pore surfaces.[68] These dependencies on pore size and chemistry do not apply to electrodialysis.

The narrow channel constriction, which acts as the reading head, is crucial for nanopore sequencing technology; however, it is not essential for ion selectivity or ion separation studies. This study elucidated that the exclusive ion selectivity originates from the surface charge of the nanopore lumen (Coulomb blockade). Therefore, we conducted an additional MD simulation of a positively charged nanopore without the narrow channel constriction; see Figure S3 (Supporting Information). As anticipated, the nanopore without the constriction also exhibits similar ion selectivity, as indicated by the average ion density inside the pore lumen. Actually, the pore without the constriction shows significantly higher water flux compared to the pore with constriction, which could lead to more efficient ion separation.

3.4. Ion Separation Under Salinity Gradients

Relying on the reverse process of electrodialysis, these charged nanopore constructions can also serve as gate-all-around nanopores, making them particularly well-suited for harnessing renewable energy from salinity gradients, widely known as blue energy generation.[69,70] Recent reports show that highly ion-selective nanopores with a gate voltage significantly increase the energy conversion efficiency under a salinity gradient.[71] It is also shown that spending minimal energy due to the gate voltage does not impair the power generation efficiency, rather the osmotic power generation is greatly enhanced through the field-strengthened perm-/selectivity.[40] In a typical reverse electrodialysis setup, seawater and freshwater are alternately passed through a stack of ion-exchange membranes. Due to the concentration gradient, the ions naturally move from seawater to freshwater. This ion movement creates an electric potential difference across the membranes, which in turn generates an electric current. In this work, we modeled the reverse electrodialysis process to showcase the potential of charged graphite-based biomimetic nanopores, revealing their capability to separate ions and possibly generate blue energy. For this, we used the same nanopore setup as in Figure 8. We initiated the simulations using the final configuration of that setup, where the saltwater was placed in the mid-chamber and the freshwater was separated, as depicted in **Figure 9**.

We begin the simulation with initial concentrations as shown in Figure 9, without applying any transmembrane voltage. Within 20 ns, we could successfully observe the ion separation and their accumulation in different channels (refer to Figure 9 at the time 20 ns). Specifically, under solely the salinity gradient, the cations are transported by the negatively-charged (cation conducting) pore to the far right chamber. Similarly, the anions are transported by the positively-charged (anion conducting) pore to the far left chamber. The corresponding accumulation of cations and anions in the terminal chambers, along with their depletion in the middle chamber, is illustrated in the bottom panel of Figure 9, showing number densities at the start (0 ns) and end (20 ns) of the simulation. Note that within 20 ns, approximately 15% of the ions have been transported. These results have been successfully reproduced in two additional simulations; see Figure S5 (Supporting Information). This transport rate can be efficiently adjusted by tuning the charging of the graphite nanopores. In fact, different absolute values of nanopore charges can potentially also induce different transport rates among the cations and the anions. These findings clearly demonstrate the potential of charged graphite-based bio-mimetic nanopores for harnessing renewable energy from salinity gradients, thus extending the use of these nanopores beyond bio-sensing, also in the field blue energy generation.

4. Conclusion

Bio-mimetic graphite-based nanopores with small constrictions are proposed and modelled in this present study with the aim to provide proof-of-principles of their high potential in diverse applications. Our comprehensive MD investigations reveal that the charge state of these nanopores renders them completely ion-selective, producing substantial EOF. We have demonstrated that the interplay of EPF and EOF facilitates the linearization of unfolded proteins and modulates the protein translocation dynamics through the nanopore, greatly enhancing the accuracy of protein detection at the single amino acid level. These findings

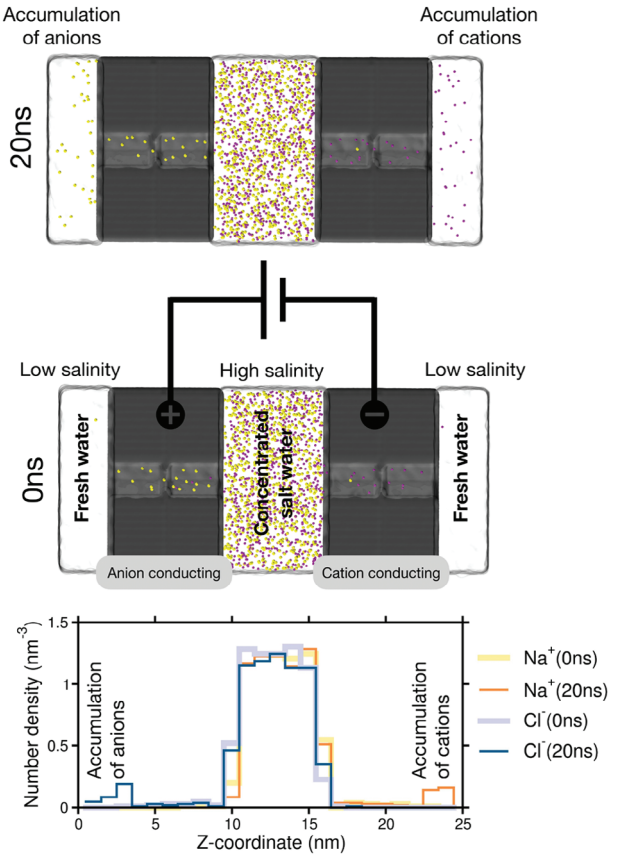

Figure 9. Top-panels. Two snapshots representing the reverse electrodialysis process, which involves separating cations and anions under salinity gradients without applying transmembrane voltage, are shown in the figure. An additional single-layer graphene sheet, which acts as a separator between the catholyte and anolyte, is not depicted in the figure. Na^+ and Cl^- ions are shown in purple and yellow spheres, respectively. Bottom panel. The number densities of cations and anions along the z-axis at the beginning and the end of the simulation as denoted in the legend.

provide pathways to further optimize the transport and detection processes. For example, the residence time of each amino acid can be increase by a selective tuning of the interplay of the EPF and EOF in order to better resolve the respective protein segment and enhance the signal-to-noise ratio. This study showcases the remarkable capability of these graphite nanopores in identifying all 20 proteinogenic amino acids and their post-translational modifications, highlighting the high sensitivity of the nanopore constriction, and are expected to be applicable to real proteins. Furthermore, we explored the significant potential of these charged bio-mimetic solid-state nanopores in seawater desalination, leveraging their complete ion-selectivity. Our electrodialysis study shows the efficient production of fresh water from seawater at a high rate. Conversely, by reversing the electrodialysis process and harnessing only the salinity gradient (without applying a transmembrane electric field), these charged nanopores can separate cations from anions, providing a platform for renewable energy solutions. These selected examples clearly provide a proof-of-principles of the robust nano/biotechnological potential of graphite-based bio-mimetic pores. We do claim here the high potential of this novel type of pores that shows promise in efficiently utilizing the interplay of the well known EOF and the EPF concepts for various applications. However, further detailed exploration is needed to fully substantiate these findings, while experimentation should verify and further develop the potential unwound here. Within this context, we anticipate that biomimetic graphitic nanopores can be synthesized using—and possibly further developing—common synthesis techniques like carbon deposition methods combined with electron-beam drilling or electrochemical reaction processes.

Supporting Information

Supporting Information is available from the Wiley Online Library or from the author.

Acknowledgements

The authors acknowledge the computing time provided in the NHR Center NHR4CES at RWTH Aachen University (project number p0020207). This was funded by the Federal Ministry of Education and Research, and the state governments participating on the basis of the resolutions of the GWK for national high performance computing at universities. This work is part of the nanodiagBW consortium (project number 03ZU1208BI) funded by the German Federal Ministry of Education and Research (BMBF) within the Clusters4Future initiative. Funding from the German Funding Agency (DFG) under the project entitled *Novel complex nanopores for the detection of natural and mutated DNA* is greatly acknowledged.

Open access funding enabled and organized by Projekt DEAL.

Conflict of Interest

The authors declare no conflict of interest.

Data Availability Statement

The data that support the findings of this study are available from the corresponding author upon reasonable request.

Keywords

blue energy, electrodialysis, Molecular Dynamics simulation, nanopore, protein sequencing

Received: September 26, 2024
Revised: October 23, 2024
Published online:

[1] P. Chen, Z. Sun, J. Wang, X. Liu, Y. Bai, J. Chen, A. Liu, F. Qiao, Y. Chen, C. Yuan, J. Sha, J. Zhang, L.-Q. Xu, J. Li, *Front. microbiol.* **2023**, *14*.
[2] D. Deamer, M. Akeson, D. Branton, *Nat. Biotechnol.* **2016**, *34*, 518.
[3] Y. Wang, Y. Zhao, A. Bollas, Y. Wang, K. F. Au, *Nat. Biotechnol.* **2021**, *39*, 1348.
[4] S. F. Mayer, C. Cao, M. Dal Peraro, *iScience* **2022**, *25*, 104145.
[5] M. Zhang, C. Chen, Y. Zhang, J. Geng, *Proteins: Struct., Funct., Bioinf.* **2022**, *90*, 1786.

[6] A. Acharya, J. D. Prajapati, U. Kleinekathöfer, *J. Phys. Chem. B* **2022**, *126*, 3995.
[7] J. Li, D. Stein, C. McMullan, D. Branton, M. J. Aziz, J. A. Golovchenko, *Nature* **2001**, *412*, 166.
[8] A. J. Storm, J. H. Chen, X. S. Ling, H. W. Zandbergen, C. Dekker, *Nat. Mater.* **2003**, *2*, 537.
[9] L. Xue, H. Yamazaki, R. Ren, M. Wanunu, A. P. Ivanov, J. B. Edel, *Nat. Rev. Mater.* **2020**, *5*, 931.
[10] Y.-L. Ying, Z.-L. Hu, S. Zhang, Y. Qing, A. Fragasso, G. Maglia, A. Meller, H. Bayley, C. Dekker, Y.-T. Long, *Nat. Nanotechnol.* **2022**, *17*, 1136.
[11] K. Motone, N. Cardozo, J. Nivala, *iScience* **2021**, *24*, 103032.
[12] A. Singh, *Nat. Methods* **2023**, *20*, 1870.
[13] F. Sanger, E. O. P. Thompson, *Biochem. J.* **1953**, *53*, 353.
[14] P. Edman, *Arch. Biochem.* **1949**, *22*, 475.
[15] Z.-L. Hu, M.-Z. Huo, Y.-L. Ying, Y.-T. Long, *Angew. Chem. Int. Ed.* **2021**, *60*, 14738.
[16] H. Ouldali, K. Sarthak, T. Ensslen, F. Piguet, P. Manivet, J. Pelta, J. C. Behrends, A. Aksimentiev, A. Oukhaled, *Nat. Biotechnol.* **2020**, *38*, 176.
[17] H. Brinkerhoff, A. S. W. Kang, J. Liu, A. Aksimentiev, C. Dekker, *Science* **2021**, *374*, 1509.
[18] S. Yan, J. Zhang, Y. Wang, W. Guo, S. Zhang, Y. Liu, J. Cao, Y. Wang, L. Wang, F. Ma, P. Zhang, H.-Y. Chen, S. Huang, *Nano Lett.* **2021**, *21*, 6703.
[19] I. C. Nova, J. Ritmejeris, H. Brinkerhoff, T. J. R. Koenig, J. H. Gundlach, C. Dekker, *Nat. Biotechnol.* **2024**, *42*, 710.
[20] G. Huang, K. Willems, M. Bartelds, P. van Dorpe, M. Soskine, G. Maglia, *Nano Lett.* **2020**, *20*, 3819.
[21] G. Huang, K. Willems, M. Soskine, C. Wloka, G. Maglia, *Nat. Commun.* **2017**, *8*, 935.
[22] M. Li, M. Muthukumar, *J. Chem. Phys* **2024**, *160*, 084905.
[23] L. Yu, X. Kang, F. Li, B. Mehrafrooz, A. Makhamreh, A. Fallahi, J. C. Foster, A. Aksimentiev, M. Chen, M. Wanunu, *Nat. Biotechnol.* **2023**, *41*, 1130.
[24] B. Mehrafrooz, L. Yu, L. Pandey, Z. S. Siwy, M. Wanunu, A. Aksimentiev, ACS Nano **2024**, DOI: 10.1021/acsnano.4c00829, (accessed: June 2024).
[25] P. Martin-Baniandres, W.-H. Lan, S. Board, M. Romero-Ruiz, S. Garcia-Manyes, Y. Qing, H. Bayley, *Nat. Nanotechnol.* **2023**, *18*, 1335.
[26] A. Sauciuc, B. Morozzo della Rocca, M. J. Tadema, M. Chinappi, G. Maglia, *Nat. Biotechnol.* **2023**, *42*, 1275.
[27] T. Ensslen, K. Sarthak, A. Aksimentiev, J. C. Behrends, *J. Am. Chem. Soc.* **2022**, *144*, 16060.
[28] M. Afshar Bakshloo, J. J. Kasianowicz, M. Pastoriza-Gallego, J. Mathé, R. Daniel, F. Piguet, A. Oukhaled, *J. Am. Chem. Soc.* **2022**, *144*, 2716.
[29] W.-H. Lan, H. He, H. Bayley, Y. Qing, *J. Am. Chem. Soc.* **2024**, *146*, 24265.
[30] K. Motone, D. Kontogiorgos-Heintz, J. Wee, K. Kurihara, S. Yang, G. Roote, O. E. Fox, Y. Fang, M. Queen, M. Tolhurst, N. Cardozo, M. Jain, J. Nivala, *Nature* **2024**, *633*, 662.
[31] K. Wang, S. Zhang, X. Zhou, X. Yang, X. Li, Y. Wang, P. Fan, Y. Xiao, W. Sun, P. Zhang, W. Li, S. Huang, *Nat. Methods* **2024**, *21*, 92.
[32] Y. Zhang, Y. Yi, Z. Li, K. Zhou, L. Liu, H.-C. Wu, *Nat. Methods* **2024**, *21*, 102.
[33] M. Zhang, C. Tang, Z. Wang, S. Chen, D. Zhang, K. Li, K. Sun, C. Zhao, Y. Wang, M. Xu, L. Dai, G. Lu, H. Shi, H. Ren, L. Chen, J. Geng, *Nat. Methods* **2024**, *21*, 609.
[34] J. Wilson, L. Sloman, Z. He, A. Aksimentiev, *Adv. Funct. Mater.* **2016**, *26*, 4830.
[35] H. Chen, L. Li, T. Zhang, Z. Qiao, J. Tang, J. Zhou, *J. Phys. Chem. C* **2018**, *122*, 2070.
[36] D. B. Wells, M. Belkin, J. Comer, A. Aksimentiev, *Nano Lett.* **2012**, *12*, 4117.
[37] Z. Ni, H. Qiu, W. Guo, *J. Phy. Chem. C* **2018**, *122*, 29380.
[38] Z. Li, Y. Qiu, K. Li, J. Sha, T. Li, Y. Chen, *J. Chem. Phys.* **2018**, *148*, 014703.
[39] M. Shankla, A. Aksimentiev, *J. Phys. Chem. B* **2017**, *121*, 3724.
[40] M. Tsutsui, W.-L. Hsu, D. Garoli, I. W. Leong, K. Yokota, H. Daiguji, T. Kawai, *ACS Nano* **2024**, *18*, 15046.
[41] G. F. Schneider, S. W. Kowalczyk, V. E. Calado, G. Pandraud, H. W. Zandbergen, L. M. K. Vandersypen, C. Dekker, *Nano Lett.* **2010**, *10*, 3163.
[42] L. Song, M. R. Hobaugh, C. Shustak, S. Cheley, H. Bayley, J. E. Gouaux, *Science* **1996**, *274*, 1859.
[43] S. Jo, T. Kim, V. G. Iyer, W. Im, *J. Comput. Chem.* **2008**, *29*, 1859.
[44] *SoftwareX* **2015**, *1-2*, 19.
[45] W. Humphrey, A. Dalke, K. Schulten, *J. Molec. Graphics* **1996**, *14*, 33.
[46] J. Wang, R. M. Wolf, J. W. Caldwell, P. A. Kollman, D. A. Case, *J. Comput. Chem.* **2004**, *25*, 1157.
[47] X. Dong, X. Yuan, Z. Song, Q. Wang, *Phys. Chem. Chem. Phys.* **2021**, *23*, 12582.
[48] P. Mark, L. Nilsson, *J. Phys. Chem. A* **2001**, *105*, 9954.
[49] G. Bussi, D. Donadio, M. Parrinello, *J. Chem. Phys.* **2007**, *126*, 014101.
[50] H. J. C. Berendsen, J. P. M. Postma, W. F. van Gunsteren, A. DiNola, J. R. Haak, *J. Chem. Phys.* **1984**, *81*, 3684.
[51] S. Páll, B. Hess, *Comput. Phys. Commun.* **2013**, *184*, 2641.
[52] T. Darden, D. York, L. Pedersen, *J. Chem. Phys.* **1993**, *98*, 10089.
[53] U. Essmann, L. Perera, M. L. Berkowitz, T. Darden, H. Lee, L. G. Pedersen, *J. Chem. Phys.* **1995**, *103*, 8577.
[54] S. Miyamoto, P. A. Kollman, *J. Comput. Chem.* **1992**, *13*, 952.
[55] B. Hess, C. Kutzner, D. van der Spoel, E. Lindahl, *J. Chem. Theory Comput.* **2008**, *4*, 435.
[56] A. Aksimentiev, J. B. Heng, G. Timp, K. Schulten, *Biophys. J.* **2004**, *87*, 2086.
[57] J. A. Maier, C. Martinez, K. Kasavajhala, L. Wickstrom, K. E. Hauser, C. Simmerling, *J. Chem. Theory Comput.* **2015**, *11*, 3696.
[58] E. R. Cruz-Chu, A. Aksimentiev, K. Schulten, *J. Phys. Chem. C* **2009**, *113*, 1850.
[59] T. Gamble, K. Decker, T. S. Plett, M. Pevarnik, J.-F. Pietschmann, I. Vlassiouk, A. Aksimentiev, Z. S. Siwy, *J. Phys. Chem. C* **2014**, *118*, 9809.
[60] Y. Ai, S. Qian, *Electrophoresis* **2011**, *32*, 996.
[61] Z. Minic, Y. Li, N. Hüttmann, G. K. Uppal, R. D'Mello, M. V. Berezovski, *Biomedicines* **2023**, *11*, 1076.
[62] A. J. Storm, C. Storm, J. Chen, H. Zandbergen, J.-F. Joanny, C. Dekker, *Nano letters* **2005**, *5*, 1193.
[63] M. Bernaschi, S. Melchionna, S. Succi, M. Fyta, E. Kaxiras, *Nano letters* **2008**, *8*, 1115.
[64] L. Gurreri, A. Tamburini, A. Cipollina, G. Micale, *Membr.* **2020**, *10*, 146.
[65] J.-M. Arana Juve, F. M. S. Christensen, Y. Wang, Z. Wei, *J. Chem. Eng.* **2022**, *435*, 134857.
[66] S. Al-Amshawee, M. Y. B. M. Yunus, A. A. M. Azoddein, D. G. Hassell, I. H. Dakhil, H. A. Hasan, *J. Chem. Eng.* **2020**, *380*, 122231.
[67] K. Decker, M. Page, A. Aksimentiev, *J. Phys. Chem. B* **2017**, *121*, 7899.
[68] M. Heiranian, A. B. Farimani, N. R. Aluru, *Nat. Commun.* **2015**, *6*, 8616.
[69] M. Graf, M. Lihter, D. Unuchek, A. Sarathy, J.-P. Leburton, A. Kis, A. Radenovic, *Joule* **2019**, *3*, 1549.
[70] R. S. Norman, *Science* **1974**, *186*, 350.
[71] J. W. Post, H. V. M. Hamelers, C. J. N. Buisman, *Environ. Sci. Technol.* **2008**, *42*, 5785.